




Article

Laser-Tracing Multi-Station Measurements in a Non-Uniform-Temperature Field

Hongfang Chen ^{*}, Ao Zhang , Mengyang Sun, Changcheng Li, Huan Wu , Ziqi Liang  and Zhaoyao Shi

Beijing Engineering Research Center of Precision Measurement Technology and Instruments, Beijing University of Technology, Beijing 100021, China; zhangao6776887@emails.bjut.edu.cn (A.Z.); smy_1204@126.com (M.S.); lichangcheng@emails.bjut.edu.cn (C.L.); wuhuane5@emails.bjut.edu.cn (H.W.); liangziqi@emails.bjut.edu.cn (Z.L.); shizhaoyao@bjut.edu.cn (Z.S.)

* Correspondence: chf0302@126.com; Tel.: +86-13401078692

Abstract: Due to the increasing requirements for the improvement of the accuracy of large coordinate-measuring machines (CMMs), the laser-tracing multi-station measurement technology, as one of the advanced precision measurement technologies, is worth studying in depth in terms of its practical application for the compensation of errors in large CMMs. Since it is difficult to maintain a constant temperature of about 20 °C in the actual workshop under the influence of solar radiation and convective heat transfer, there is a gradient in the spatial temperature distribution, and the overall temperature changes with the influence of external factors with synchronous hysteresis, it is difficult for the actual calibration environment to meet the standard environmental requirements. Therefore, the influence of temperature and other environmental factors on the accuracy of laser ranging and large-scale CMM calibration should not be ignored. In this paper, on the basis of analyzing the temperature distribution and change rule of large CMM measurement space under different working conditions, the radial basis function (RBF) neural network algorithm was used to build a non-uniform-temperature field model, and based on this model and the measurement principle of the laser-tracking instrument, the method of laser tracking and interferometric ranging accuracy enhancement was put forward under a non-uniform-temperature field. Finally, based on the multi-station technique of laser tracing, an accurate solution for the volumetric error of large CMMs under the condition of non -20 °C ambient temperature was realized. Simulation results proved that compared with the traditional temperature-compensation method, the proposed method improved the measurement accuracy of the volumetric error of a large-scale CMM using laser-tracing multi-station technology in a non-uniform-temperature field by 33.5%. This study provides a new approach for improving the accuracy of laser-tracer multi-station measurement systems.

Keywords: large-scale CMM; multi-station measurement technology; non-uniform-temperature field; laser tracer



Citation: Chen, H.; Zhang, A.; Sun, M.; Li, C.; Wu, H.; Liang, Z.; Shi, Z. Laser-Tracing Multi-Station Measurements in a Non-Uniform-Temperature Field. *Photonics* **2024**, *11*, 727. <https://doi.org/10.3390/photonics11080727>

Received: 18 July 2024

Revised: 30 July 2024

Accepted: 2 August 2024

Published: 4 August 2024



Copyright: © 2024 by the authors. Licensee MDPI, Basel, Switzerland. This article is an open access article distributed under the terms and conditions of the Creative Commons Attribution (CC BY) license (<https://creativecommons.org/licenses/by/4.0/>).

1. Introduction

Coordinate-measuring machines (CMMs) are characterized by their high versatility, automation, and measurement accuracy [1]. Large-scale CMMs are commonly applied for the measurement of complex workpiece surfaces such as precision castings, automotive housings, and aircraft blades. The requirements for manufacturing accuracy have been increasing owing to developments in the manufacturing industry. Therefore, the calibration and alignment of large-scale CMMs are important. Quick and accurate calibration of CMMs, including detecting and compensating for CMM various errors, is one of the important ways to improve the measurement accuracy of CMM [2].

Geometric errors are an important source of error in CMMs. Aguado et al. [3,4] proposed a compensation technique based on a nonlinear optimization method to indirectly measure the geometrical error of a machine tool using three laser trackers, using regression

analysis to characterize the geometrical error of the machine tool. However, its method is highly affected by measurement noise, measurement point distribution, and optimization constraints of polynomial regression and is time-consuming. Jindong Wang [5] and others used a sequential multilateral technique to detect the geometric error of multi-axis CNC machine tools. As only one laser tracker is used, it greatly reduces the cost and has high measurement accuracy by using only length quantities in the measurement process. However, their geometric errors are obtained by iterative calculation, which is time-consuming.

A laser tracer is a special device used for calibrating a CMM, and its measurement accuracy reaches $0.2 \mu\text{m} + 0.3L \mu\text{m}/\text{m}$. Therefore, a laser tracer is more suitable for error compensation in large-scale CMMs. Schwenke et al. [6] used laser tracers to calibrate machine tools based on the multilateral method, which requires the simultaneous use of four laser tracers. However, the high cost of these four laser tracers limits the application of multilateral measurement techniques. Camboulives et al. [7] proposed a technique for measuring the CMM volumetric error using one laser tracer at multiple stations. A single laser tracer was used to establish a reference measurement system based on the measurements at successive positions, and the 3D coordinates of the point to be measured were obtained according to the multilateral measurement principle. Thus, the measurement cost is significantly reduced; however, the measurement method is time-consuming for time-shifting multi-station calibration.

Owing to the difficulties in meeting standard environmental requirements [8–11], it is difficult to maintain a standard constant temperature of $20 \text{ }^\circ\text{C}$ under the influence of factors such as solar radiation and convective heat transfer in workshops, where a spatial temperature distribution gradient exists. Furthermore, the overall temperature change is synchronized with external factors in a lagged manner. When temperature and other environmental parameters deviate from standard conditions, the effects of temperature deviation on the accuracy of laser ranging and the compensation accuracy of geometric errors with laser-tracing multi-station technology in large-scale CMMs cannot be ignored. Zhang [1] believed that two main methods could be used to reduce the temperature error: temperature control and temperature error compensation. In the temperature control method, multi-layer constant-temperature control measures can be used: constant-temperature building, constant-temperature room, constant-temperature hood, and other multi-layer constant-temperature methods. In addition, a beam passes through helium for constant-temperature measurements to reduce the influence of environmental parameters on the refractive index of the medium. Joo et al. [12] described combined methods of displacement heterodyne laser interferometry and wavelength tracking based on a Fabry–Perot cavity to correct the instantaneous wavelength in air and experimentally realized a difference of 2 nm compared with the results of traditional equation-based techniques. He et al. [13] mainly ascribed the errors in laser comparators to the temperature distribution and guideway straightness and compensated for the displacement measurement of laser interferometers according to Edlén's equation. Zhu et al. [14] pointed out that environmental factors, especially inhomogeneous temperature, could lead to considerable measurement uncertainty and proposed to optimize the configuration of the laser tracker station for large components in a non-uniform-temperature field using Monte Carlo methods. Ting Li et al. [15] utilized a laser tracker located in an underground laboratory to experimentally verify that the measurement accuracy can be improved by refractive index compensation under air conditioning with temperature control and off air conditioning in the natural condition (the average maximum change in air temperature is $\Delta T_1 = 0.237 \text{ }^\circ\text{C}/\text{h}$ and $\Delta T_2 = 0.022 \text{ }^\circ\text{C}/\text{h}$, respectively). And higher measurement accuracy can be obtained in the natural state with the air conditioner turned off, proving that the stability of the laboratory environmental conditions is one of the keys to improve the accuracy of a large-size measurement device. Aguilar et al. [16] designed a high-precision trilinear telescopic system with a measurement principle based on simultaneous laser multipoint positioning, which significantly reduced the time required for data acquisition and improved the measurement accuracy by avoiding the effects of machine repeatability and temperature

variations between cycles. Zeng et al. [17] addressed the key issue of laser-tracker application in unstable environments, such as non-uniform-temperature fields, and proposed and verified a measurement error compensation method based on an error similarity analysis. Pisani Marco et al. [18] used an acoustic thermometer to measure air temperature along the measurement path of an interferometer, realized an accuracy of 0.1 °C and a maximum measurement distance of up to 11 m, and demonstrated the potential of this method in measuring the vertical temperature gradient. Wu et al. [19] experimentally modeled a non-uniform refractive index field, simulated the propagation path of light in the non-uniform refractive index field using the Runge–Kutta ray-tracing method, and successfully obtained the aberration displacement of the imaging plane. In turn, by compensating for the distortion offset of the imaging plane, the correction of the light affected by the variable refractive index field was realized, reducing the visual measurement distortion caused by the change of the refractive index gradient.

To avoid the influence of environmental factors such as temperature, calibration personnel should develop an optimal calibration scheme according to the actual environment so that the calibration results can indicate the actual measurement accuracy of the calibrated instrument [8]. Temperature compensation for laser-tracing multi-station technology has not yet been reported. Owing to the large measurement space of large-scale CMMs, uneven and time-varying spatial temperature distributions, and time-consuming multi-station measurements of laser tracers, the effect of temperature on interferometric ranging with a laser tracer cannot be ignored. To address these problems, a temperature-compensation method for laser-tracing multi-station measurements in a non-uniform-temperature field is proposed in this paper. The laser beam range is equally spaced and subdivided, and a model of the non-uniform-temperature field is established based on the RBF neural network to estimate the ambient temperature in the CMM measurement space. The estimation results indicate that the accuracy of the laser-tracing multi-station measurement method was improved. The proposed method is characterized by its low cost, simple operation, and high flexibility.

2. Materials and Methods

A laser tracer should work in an ideal working environment at 20 °C so as to guarantee its measurement accuracy. However, the ambient temperature is affected by thermal expansion/contraction, gravity, and buoyancy. Even external devices, such as air conditioners, are used to control the ambient temperature to realize a uniform temperature distribution.

To explore the effect of temperature on the refractive index and laser ranging, a non-uniform-temperature field model based on an RBF neural network was established in this study. The stepwise compensation idea was adopted in the temperature compensation of the laser-tracking measurement results to improve the accuracy of the laser-tracing multi-station measurements. In this way, the accuracy improvement of the CMM volumetric error was realized based on the laser-tracing multi-station technology. A flowchart of the error compensation for large-scale CMMs based on a non-uniform-temperature field is shown in Figure 1.

2.1. Effect of Temperature on Laser Interferometric Ranging

The distance measurement principle of laser tracers is based on laser interferometric ranging. Laser tracers are highly accurate. Although the wavelength emitted by the laser itself cannot be affected by small changes in the operating environment, environmental conditions (temperature, humidity, air pressure, etc.), especially changes in the refractive index of the air, affect the propagation of the laser through the medium. Interference patterns or fringes can be affected by a temperature variation, which in turn affects the accuracy of interferometric measurements. The CMM workspace is nonideal and variable. Therefore, the performance of environmental compensation systems is particularly important. In current environmental compensation systems, the temperature, humidity, and air pressure measurements obtained using a single sensor are directly used as environmental param-

eters. The actual workshop environment is complex and variable, and the temperature distribution in the CMM workspace is non-uniform and varies with time. Therefore, when a laser tracer is used for multi-station measurements, the optical path of the laser tracer propagates across the temperature gradient, and the influence of the refractive index on the wavelength cannot be ignored [20].

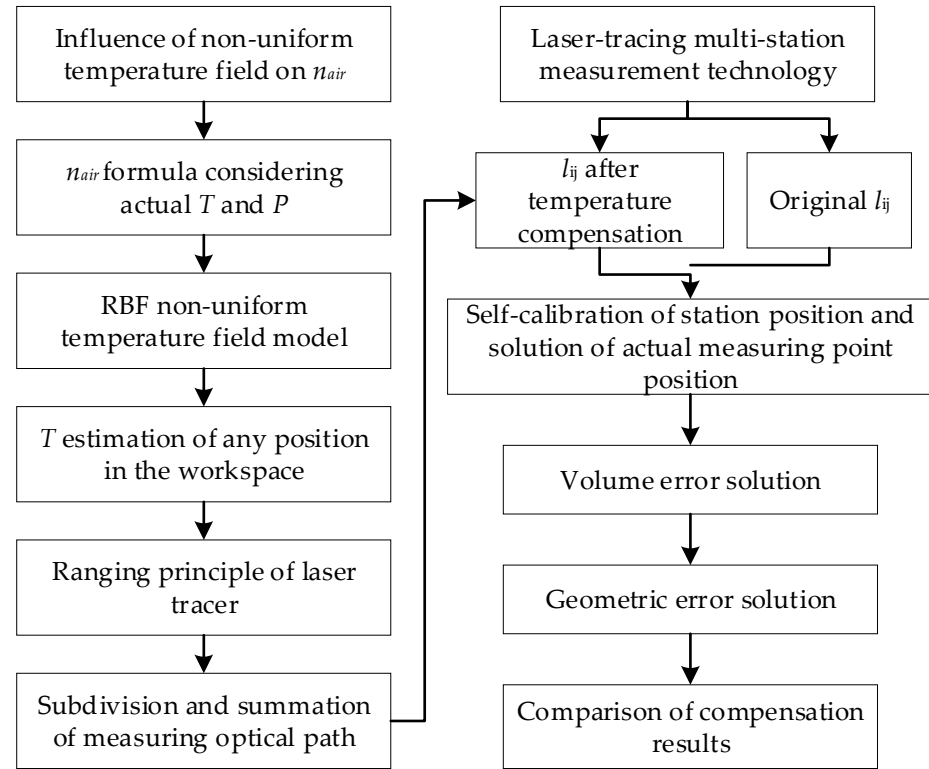


Figure 1. Flow chart of error compensation for large-scale CMMs based on a non-uniform-temperature field.

The coordinates of any point in the CMM workspace are set to $A_i(x_i, y_i, z_i)$, $i = 1, 2, 3, \dots, n$. The temperature at this point is T_i . Then, the refractive index of air at point A_i is expressed as follows [21]:

$$n_i = 1 + \left[\frac{(n_s - 1)P}{96\,095.43} \right] \left[\frac{1 + 10^{-8}(0.601 - 0.00972T_i)P}{1 + 0.003661T_i} \right] \quad (1)$$

where n_s is the refractive index of air in the standard state, and P is the ambient pressure. When only the effect of the temperature change on the refractive index is considered, the change in the refractive index can be expressed as follows:

$$\partial n_i = \left[\frac{(n_s - 1)P}{96\,095.43} \right] \left\{ \frac{-0.00972P(1 + 0.003661T_i) \times 10^{-8} - 0.003661[1 + 10^{-8}(0.601 - 0.00972T_i)P]}{(1 + 0.003661T_i)^2} \right\} \partial T_i \quad (2)$$

According to the actual working environment, the Edlén equation is used to calculate the standard refractive index, $n_s = 1.0002765$. In the vicinity of the normal state (air pressure $P = 101,325$ Pa; temperature $T = 20$ °C; relative humidity $h = 50\%$), Equation (2) can be simplified:

$$\frac{\partial n_i}{\partial T_i} = -9.297 \times 10^{-7} \quad (3)$$

When only the effect of the temperature change on the wavelength is considered, the change in wavelength can be expressed as follows:

$$\begin{aligned} \partial\lambda_i &= -\frac{\lambda_0}{n_i^2} \partial n_i = 5.880 \times 10^{-4} \partial T_i \\ \frac{\partial\lambda_i}{\partial T_i} &= 5.880 \times 10^{-4} \text{ nm}/^\circ\text{C} \end{aligned} \quad (4)$$

The laser-tracer ranging equation can also be simplified:

$$L = \frac{\lambda}{2} N \quad (5)$$

where λ is the wavelength of laser propagation in the medium, and N is the value of the stripe count. When only the effect of temperature change on laser interferometric ranging is considered, the change in laser interferometric ranging can be expressed:

$$\begin{aligned} \partial L_i &= \frac{\partial\lambda_i}{2} N = 2.940 \times 10^{-4} N \partial T_i \\ \frac{\partial L_i}{\partial T_i} &= 4.646 \times 10^{-7} \text{ m}/^\circ\text{C} \end{aligned} \quad (6)$$

2.2. Non-Uniform-Temperature Field Model Based on RBF Neural Network

The laser-tracer multi-station measurement system facilitates the error measurement of a large-scale CMM. The CMM workspace is large, and the spatial distribution of the temperature is uneven. In addition, an overall synchronized temporal temperature variation caused by temperature and other effects also exists. The CMM is a precision measurement instrument, and its measurement process involves motion along three axes. However, it is difficult to arrange multiple fixed-temperature sensors in the measurement space. Therefore, in the study of non-uniform-temperature fields in the CMM workspace, it is necessary to predict the temperature in the workspace. Based on an RBF neural network, a model of the non-uniform-temperature field in the CMM measurement space was developed in this study. Compared to complex mathematical models, the RBF neural network can more efficiently and conveniently estimate the temperature at any point in space.

The RBF neural network-based non-uniform-temperature field model of the CMM measurement space established in this study is shown in Figure 2. The network is composed of three layers: input, hidden, and output. For a non-uniform-temperature field at a certain time, the parameters (x_i , y_i , and z_i) of the input layer are the 3D coordinates of any point A_i in the CMM workspace. The parameters x_i , y_i , z_i , and t_i of the input layer are the 3D coordinates of A_i and time data. The radial basis function activation function used in this study is the Gaussian function [22]. Let \mathbf{X}_i be the RBF input sample vector. The activation function $\varphi(\mathbf{X}_i, \mathbf{c}_j)$ of the hidden layer neurons is given by the Gaussian function, which is defined as follows:

$$\varphi_j(\mathbf{X}_i, \mathbf{c}_j) = \exp\left(-\frac{1}{2\delta_j^2} \|\mathbf{X}_i - \mathbf{c}_j\|^2\right) \quad (7)$$

where \mathbf{c}_j is the central vector of the basis function, referring to the center position of the radial basis function in the input space; δ_j is the width vector of the basis function, referring to the magnitude of the width of the radial basis function; \mathbf{X}_i is the i -th input vector ($\mathbf{X}_i(x_i, y_i, z_i)$ or $\mathbf{X}_i(x_i, y_i, z_i, t_i)$); and the output layer T_i is a temperature or temperature-dependent function that is equal to the linear combination of the RBF output as the basis function:

$$T_i = \sum_{j=1}^m \omega_j \varphi_j(\mathbf{X}_i, \mathbf{c}_j) \quad (8)$$

where ω_j is the connection weight between the hidden and output layers. The implementation steps are as follows. First, the weights, center vector, and width vector are initialized. Second, the output value of the hidden layer is calculated. Subsequently, the value of the

output layer is calculated. Next, the mean squared error is calculated. Finally, the initial parameters are updated using the gradient descent method.

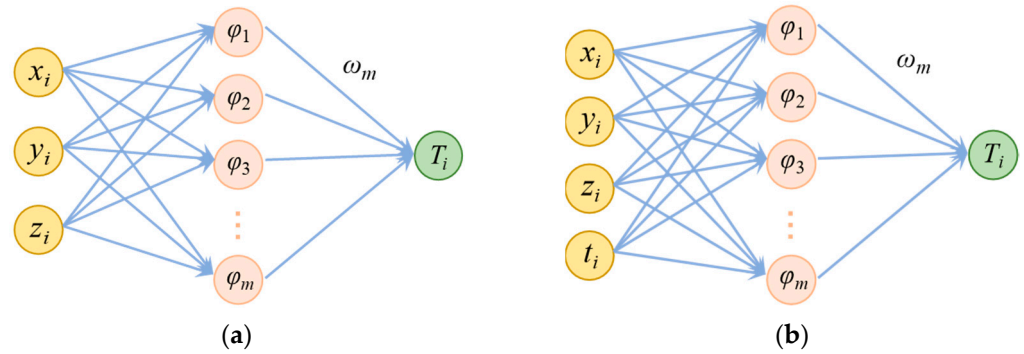


Figure 2. (a) Non-uniform-temperature field RBF model; (b) non-uniform-temperature field RBF model with time variables.

By comparing the output layer values, which are calculated after introducing the initialized parameters, with the target values, the loss function is represented by the mean squared error:

$$E = \frac{1}{2n} \sum_{i=1}^n (T_i(\mathbf{X}_i) - T_i)^2 \tag{9}$$

where $T_i(\mathbf{X}_i)$ is the output temperature calculated from the input of the i -th sample; T_i is the target output temperature corresponding to the input of the i -th sample.

2.3. Laser-Tracing Multi-Station Measurement Model with Temperature Compensation

A multi-station measurement model based on a single laser tracer was established using a redundant measurement method. The laser tracer was placed at different positions on the CMM measurement platform in a time-shifted manner. The cat’s eye reflector was moved together with the CMM probe, as shown in Figure 3. The laser from the laser tracer was reflected by the cat’s eye and then reflected by the standard sphere fixed inside the laser tracer as the measurement beam, thus interfering with the reference beam. In this manner, the tracking and ranging of the laser tracer were realized. The multi-station measurement experimental device of laser tracer is shown in the Figure 4.

It was assumed that a laser tracer was used to measure n planned measurement points in the CMM measurement space at m stations. The coordinates of the n measurement points are $A_i(x_i, y_i, z_i)$, $i = 1, 2, 3, \dots, n$. The station coordinates of the laser tracer are $P_j(X_j, Y_j, Z_j)$, $j = 1, 2, 3, \dots, m$. The redundant error of the laser tracer is d_j . The relative interference length of the cat’s eye reflector during the measurement process is l_{ij} . The distance between two points in 3D space is expressed in [23] as follows:

$$\sqrt{(x_i - X_j)^2 + (y_i - Y_j)^2 + (z_i - Z_j)^2} = d_j + l_{ij} \tag{10}$$

The working principle of a laser tracer is interferometry. The reference beam interferes with the measurement beam, and the counting stripe varies with the movement of the cat’s eye. The measurement distance equation for a laser tracer is expressed as follows:

$$l_{ij} = \frac{\lambda}{2} N, \lambda = \frac{\lambda_0}{n_{air}} \tag{11}$$

where λ_0 is the laser wavelength in the standard environment, and n_{air} is the air refractive index in the actual environment.

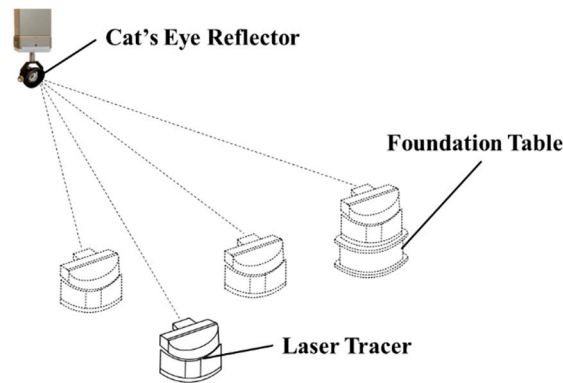


Figure 3. Laser-tracing multi-station measurement system.

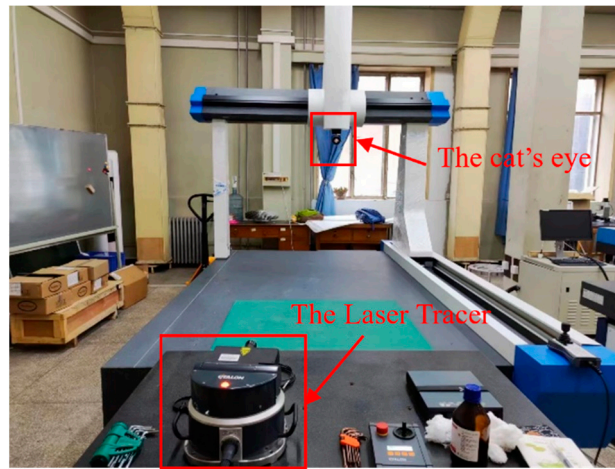


Figure 4. The multi-station measurement experimental laser-tracer device.

At time t_i , the cat's eye moves with the CMM to measurement point $A_i(x_i, y_i, z_i)$, and the temperature at point A_i is T_i . The refractive index of the air at A_i is expressed by Equation (1).

If the laser path is subdivided into p segments, as shown in Figure 5, the air refractive index of each path is $n_k, k = 1, 2, \dots, p$; the temperature field at moment t_i can be derived from the RBF model described by n_k as follows:

$$n_k = 1 + \left[\frac{(n_s - 1)P}{96\,095.43} \right] \left[\frac{1 + 10^{-8}(0.601 - 0.00972T_k)P}{1 + 0.003661T_k} \right] \quad (12)$$

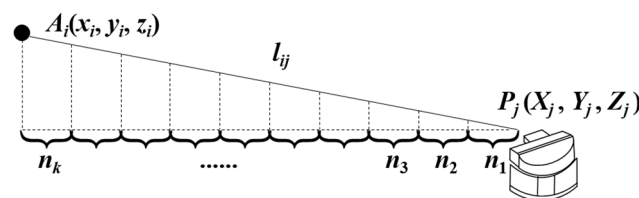


Figure 5. Ranging optical path subdivision model of a laser tracer.

Then, the interferometric length value l_{ij}' after temperature compensation can be expressed:

$$l_{ij}' = \frac{1}{p} \sum_{k=1}^p \frac{\lambda_0}{2n_k} N = \frac{\lambda_0 N}{2p} \sum_{k=1}^p \frac{1}{n_k} \quad (13)$$

In previous laser-tracing multi-station measurement methods, the influence of the non-uniform-temperature field was usually ignored, and the refractive index was believed

to be a fixed value throughout the measurement optical path of laser interferometry. Thus, the refractive index in the measurement range was n_u . Then, the distance measurement value can be expressed as follows:

$$l_u = \frac{\lambda_0}{2n_u} N \tag{14}$$

The ratio of the laser interferometric lengths obtained before and after the compensation temperature r_{ij} is thus expressed:

$$r_{ij} = \frac{l_u}{l_{ij}'} = \frac{\frac{\lambda_0}{2n_u} N}{\frac{\lambda_0 N}{2p} \sum_{k=1}^p \frac{1}{n_k}} = \frac{p}{n_u \sum_{k=1}^p \frac{1}{n_k}} \tag{15}$$

Therefore, the laser interferometric ranging error caused by neglecting the influence of the non-uniform-temperature field in the CMM workspace can be expressed as $e = l_{ij} \cdot (r_{ij} - 1)$.

After substituting l_{ij}' into the laser-tracing multi-station measurement model, the coordinates of the laser-tracer stations and the actual coordinates of the measurement point after temperature compensation can be obtained. Finally, the CMM volumetric error measurement results are obtained after temperature compensation.

To solve the coordinates of laser tracer's station $P_j (X_j, Y_j, Z_j)$ and the redundant error d_j of the laser tracer, the objective function of the nonlinear least-squares problem is obtained using the laser-tracer multi-station measurement model as follows:

$$F(X_j, Y_j, Z_j, d_j) = \sqrt{(x_i - X_j)^2 + (y_i - Y_j)^2 + (z_i - Z_j)^2} - d_j - l_{ij} \tag{16}$$

Using the Levenberg–Marquardt (L–M) algorithm, self-calibration of the laser-tracer station was performed to calibrate the coordinates of the laser-tracer station $P_j (X_j, Y_j, Z_j)$ and the redundant error d_j of the laser tracer.

Similarly, taking the station coordinates and redundant points obtained above as the known conditions, the actual values of the measurement points $A_i(x_i, y_i, z_i)$, $A_i'(x_i', y_i', z_i')$ can be solved using the laser-tracking multi-station measurement model and the L–M algorithm. According to the equation for the distance between two points in the laser-tracing multi-station measurement system (Equation (10)), the objective equation of the L–M algorithm is expressed as follows:

$$F(x_j, y_j, z_j) = \sqrt{(x_i - X_j)^2 + (y_i - Y_j)^2 + (z_i - Z_j)^2} - d_j - l_{ij} \tag{17}$$

Ideally, the CMM should move to the measurement point with the theoretical coordinates $A_i(x_i, y_i, z_i)$. However, under the influence of manufacturing, installation, elastic deformation, and thermal deformation of the CMM, the volumetric error and the difference between the actual coordinates $A_i'(x_i', y_i', z_i')$ and the theoretical coordinates $A_i(x_i, y_i, z_i)$ of the CMM measurement point can be expressed as follows:

$$\begin{bmatrix} \Delta x_i \\ \Delta y_i \\ \Delta z_i \end{bmatrix} = \begin{bmatrix} x_i' \\ y_i' \\ z_i' \end{bmatrix} - \begin{bmatrix} x_i \\ y_i \\ z_i \end{bmatrix} \tag{18}$$

The relationship between the volumetric and geometric errors is established using a quasi-rigid body model [24]. Then, a system of objective equations containing known volumetric errors is obtained to solve these geometric errors. Subsequently, 21 geometric error terms of the CMM are solved using the elastic network algorithm and QR decomposition method.

For CMMs with different structures and motion modes, a total of 24 different quasi-rigid body models are available. In this study, using an FXYZ-type CMM as an example, a quasi-rigid body model is established as follows:

$$\begin{aligned}
 \Delta x &= \delta_x(x) + \delta_x(y) + \delta_x(z) - \alpha_{xy} \times y - \alpha_{xz} \times z - \varepsilon_z(x) \times y + [\varepsilon_y(x) + \varepsilon_y(y)] \times z \\
 &\quad - [\varepsilon_z(x) + \varepsilon_z(y) + \varepsilon_z(z)] \times y_p + [\varepsilon_y(x) + \varepsilon_y(y) + \varepsilon_y(z)] \times z_p \\
 \Delta y &= \delta_y(x) + \delta_y(y) + \delta_y(z) - \alpha_{yz} \times z - [\varepsilon_x(x) + \varepsilon_x(y)] \times z \\
 &\quad + [\varepsilon_z(x) + \varepsilon_z(y) + \varepsilon_z(z)] \times x_p - [\varepsilon_x(x) + \varepsilon_x(y) + \varepsilon_x(z)] \times z_p \\
 \Delta z &= \delta_z(x) + \delta_z(y) + \delta_z(z) + \varepsilon_x(x) \times y - [\varepsilon_y(x) + \varepsilon_y(y) + \varepsilon_y(z)] \times x_p \\
 &\quad + [\varepsilon_x(x) + \varepsilon_x(y) + \varepsilon_x(z)] \times y_p
 \end{aligned} \tag{19}$$

where $A_1(x_p, y_p, z_p)$ are the coordinates of the initial point to be measured; (x, y, z) is the displacement of CMM relative to the initial point; $(\Delta x, \Delta y, \Delta z)$ is the volumetric error of the point to be measured; $\delta_x(x)$ is the x -axis positioning error; $\delta_y(x)$ and $\delta_z(x)$ are the x -axis straightness motion errors; $\varepsilon_x(x)$, $\varepsilon_y(x)$, and $\varepsilon_z(x)$ are the x -axis angular motion errors; $\delta_y(y)$ is the y -axis positioning error; $\delta_x(y)$ and $\delta_z(y)$ are the y -axis straightness motion errors; $\varepsilon_x(y)$, $\varepsilon_y(y)$, and $\varepsilon_z(y)$ are the y -axis angular motion errors; $\delta_z(z)$ is the z -axis positioning error; $\delta_x(z)$ and $\delta_y(z)$ are the z -axis straightness motion errors; $\varepsilon_x(z)$, $\varepsilon_y(z)$, and $\varepsilon_z(z)$ are the z -axis angular motion errors; and α_{xy} , α_{xz} , and α_{yz} are verticality errors.

According to the quasi-rigid body model above, the system of equations between the volumetric and geometric errors is established with the number of points to be measured and the number of errors. Let the displacement from any point $A_1(x_p, y_p, z_p)$ to the first point $A_i(x_i, y_i, z_i)$ in the CMM measurement space be $x_{i1} = x_i - x_p$, $y_{i1} = y_i - y_p$, and $z_{i1} = z_i - z_p$. Substituting the displacement into the quasi-rigid body model of the CMM (Equation (19)) yields the following:

$$A_i \mathbf{x}_i = \mathbf{b}_i \tag{20}$$

$$A_i = \begin{bmatrix}
 1 & 0 & 0 & 0 & z_{i1} + z_p & -y_{i1} - y_p & 1 & 0 & 0 & 0 & z_{i1} + z_p & -y_p & 1 & 0 & 0 & 0 & z_p & -y_p & -y_{i1} & -z_{i1} & 0 \\
 0 & 1 & 0 & -z_{i1} - z_p & 0 & x_p & 0 & 1 & 0 & -z_{i1} - z_p & 0 & x_p & 0 & 1 & 0 & -z_p & 0 & x_p & 0 & 0 & -z_{i1} \\
 0 & 0 & 1 & y_p & -x_p & 0 & 0 & 0 & 1 & y_p & -x_p & 0 & 0 & 0 & 1 & y_p & -x_p & 0 & 0 & 0 & 0
 \end{bmatrix} \tag{21}$$

$$\mathbf{x}_i = \begin{bmatrix}
 \delta_x(x) & \delta_y(x) & \delta_z(x) & \varepsilon_x(x) & \varepsilon_y(x) & \varepsilon_z(x) & \delta_x(y) & \delta_y(y) & \delta_z(y) & \varepsilon_x(y) \\
 \varepsilon_y(y) & \varepsilon_z(y) & \delta_x(z) & \delta_y(z) & \delta_z(z) & \varepsilon_x(z) & \varepsilon_y(z) & \varepsilon_z(z) & \alpha_{xy} & \alpha_{xz} & \alpha_{yz}
 \end{bmatrix}^T \tag{22}$$

$$\mathbf{b}_i = [\Delta x_i, \Delta y_i, \Delta z_i]^T \tag{23}$$

The coefficient matrix of Equation (20) is a singular matrix. Therefore, it can be solved using the elastic network algorithm [25] with the following optimization objective:

$$\begin{aligned}
 \hat{x}^{Elastic\ net} &= \underset{x}{\operatorname{argmin}} \frac{1}{2} \|\mathbf{b} - \mathbf{A}\mathbf{x}\|^2 \\
 \text{subject to} & (1 - \alpha) \sum_{k=1}^f |x_k| + \alpha \sum_{k=1}^f x_k^2 \leq t
 \end{aligned} \tag{24}$$

where $\hat{x}^{Elastic\ net}$ is the elastic network optimization objective; \mathbf{b} is the CMM volumetric error; \mathbf{A} is the coefficient matrix of the objective equation system of the quasi-rigid body model; α is the penalty factor of the elastic network algorithm; k is the k -th geometric error, $k = 1, 2, 3, \dots, f$; f is the number of geometric errors to be solved; and t is the reconciliation parameter ($t \geq 0$). The coordinate descent method, or Lagrangian duality, is used to solve the elastic network. The coefficients of the four angular motion errors $\varepsilon_z(y)$, $\varepsilon_x(z)$, $\varepsilon_y(z)$, $\varepsilon_z(z)$ comprise the coordinates of the initial measurement point, which is the origin of these coordinates. Therefore, only 17 geometric errors can be solved using an elastic network algorithm. The angular motion error $\varepsilon_z(y)$, $\varepsilon_x(z)$, $\varepsilon_y(z)$, $\varepsilon_z(z)$ is obtained based on the geometric model of the volumetric and uniaxial geometric errors by QR decomposition.

3. Simulation Experiment Analysis

3.1. Setting of Simulation Experiments

For the CMM workspace required for the experiment, a simplified laboratory model was established using SolidWorks (Figure 6). Its size was $14\text{ m} \times 8\text{ m} \times 3.5\text{ m}$. The object to be explored was the left CMM with a workspace range of $2800\text{ mm} \times 1200\text{ mm} \times 800\text{ mm}$, and the right CMM was used for comparison. The CMM used in the experiment was developed by Beijing Aviation Precision Machinery Research Institute of China Aviation Industry Corporation (AVIC), model FUTURE 301515, with a signal value error of $MPE_E = (4.0 + 4.0 L/1000)\text{ }\mu\text{m}$. The laser tracer was developed by Etalon, model 072009TRIF, and the spatial measurement uncertainty of the laser tracer was $u_{Laser\ Tracer}(l_{ij}) = 0.2\text{ }\mu\text{m} + 0.3 \cdot L\text{ }\mu\text{m/m}$. The temperature of the experimental environment was numerically simulated using the ANSYS FLUENT software. The laboratory environment was as follows. First, convective heat transfer occurred between only one wall (including three windows) and the outdoor environment. Second, two indoor air-conditioning cabinets were used to maintain a constant temperature. The laboratory was affected by solar radiation, as the season was summer. The indoor fluid was air with a low flow velocity, which was considered both an incompressible fluid and a steady-state Newtonian viscous fluid. The turbulence model is applicable to solve this problem, and here, the standard $k\text{-}\epsilon$ model proposed by Launder and Spalding in 1972 was adopted [26].

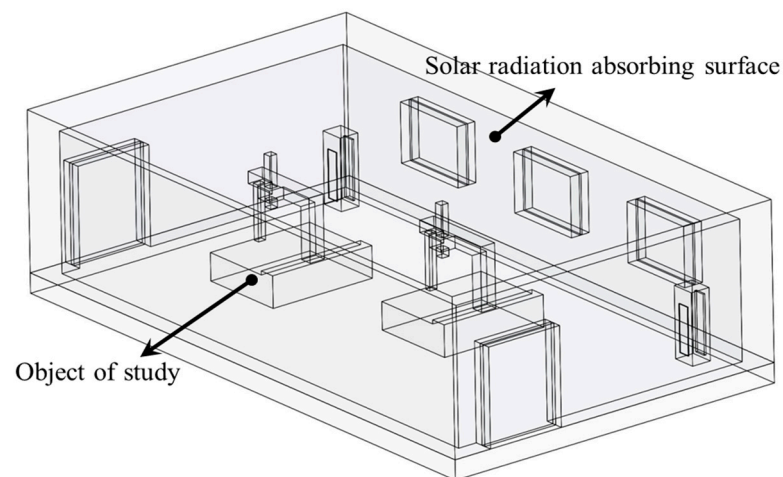


Figure 6. Simulation environment.

The indoor air flows at low velocities, and the fluid pressure changes are small. The characteristics of indoor air were in accordance with the Boussinesq assumption. Therefore, the change in air density caused by temperature change was mainly considered in the simulation environment. The other physical parameters of the air fluid do not change with the density, and only gravity-related terms were considered in the momentum equation. The densities of the remaining terms were treated as constant. A set of fluid-motion equations based on the Boussinesq assumption, called the Boussinesq set of equations, was adopted. The density in the gravity term in the equation can be expressed as follows (air density expression) [27]:

$$\rho = \rho_0[1 - \beta(T - T_0)] \quad (25)$$

where ρ is the density of the fluid (air) gravity term, ρ_0 is the air reference density (at T_0), and β is the coefficient of thermal expansion.

When fluid flow and heat-transfer problems are solved using numerical simulation methods, basic control equations (basic laws) should be considered. The basic laws of

fluid flow include the laws of conservation of mass, momentum, and energy. The control equations are as follows [27]:

$$\frac{\partial(\rho\varphi)}{\partial t} + \text{div}(\rho U\varphi) = \text{div}(\Gamma \text{grad}\varphi) + S \tag{26}$$

where φ is a generic variable (u, v, ω, T , etc.); Γ is the generalized diffusion coefficient; S is the generalized source term.

The semi-implicit method for pressure-linked equations (SIMPLE) algorithm was selected for the numerical simulation, and the following two cases were considered:

1. The parameters of the air-conditioned cabinet were set as follows: wind speed of 1.5 m/s, air supply volume of 1300 m³/h, air temperature of 20 °C (fixed temperature), and initial indoor temperature of 16 °C. In addition, solar radiation was also considered;
2. Under the condition of natural convection (the air-conditioned cabinet is off), the initial room temperature was 16 °C, and solar radiation was considered.

The numerical simulation results are shown in Figures 7 and 8. When the air-condition cabinets were used to fix the temperature, the temperature distribution was complex, and horizontal and vertical temperature differences existed. The constant-temperature effect was evident, and the temperature gradient was small. The temperature distributions in the CMM workplace in the two cases indicated that the horizontal temperature gradient of the CMM workspace could be reduced by increasing the distance between the air-condition cabinet and CMM. In the second case, the temperature distribution was relatively simple, and only the vertical temperature difference was considered, as proposed in the Boussinesq assumption. The temperature gradient was large and related to the difference between the indoor and outdoor temperatures.

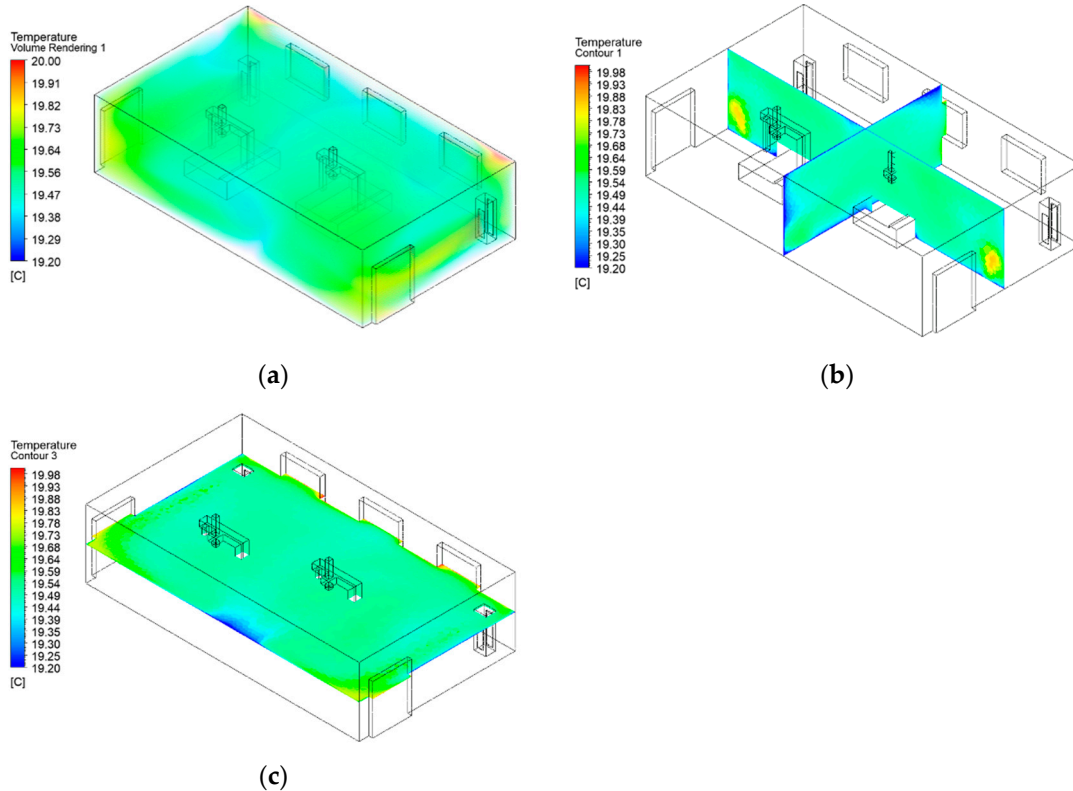


Figure 7. Numerical simulation for the fixed-temperature case: (a) overall temperature distribution; (b) vertical cross-section; (c) horizontal cross-section.

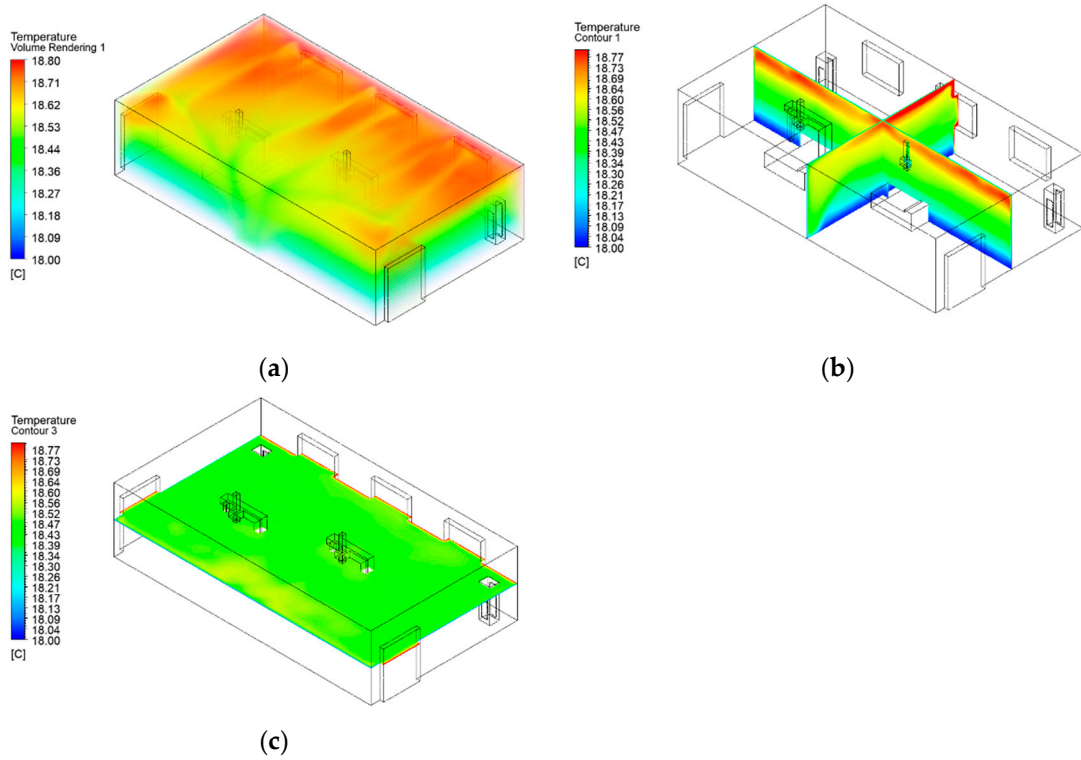


Figure 8. Numerical simulation of natural convection conditions: (a) overall temperature distribution; (b) vertical cross-section; (c) horizontal cross-section.

The spatial temperature data from the above numerical simulations were saved for the subsequent training and validation of the RBF-based non-uniform-temperature field model.

3.2. Validation of the Non-Uniform-Temperature Field Model

The laser-tracing multi-station measurement system was only used for the CMM error measurement; therefore, this study focused on the CMM workspace temperature field. The temperature data of the left CMM workspace used in this study were screened and used as the training samples. In total, 226 nodes were screened (Figure 9). The accuracy of the temperature sensor PT100 is $\pm(0.15 + 0.002) \text{ }^\circ\text{C}$.

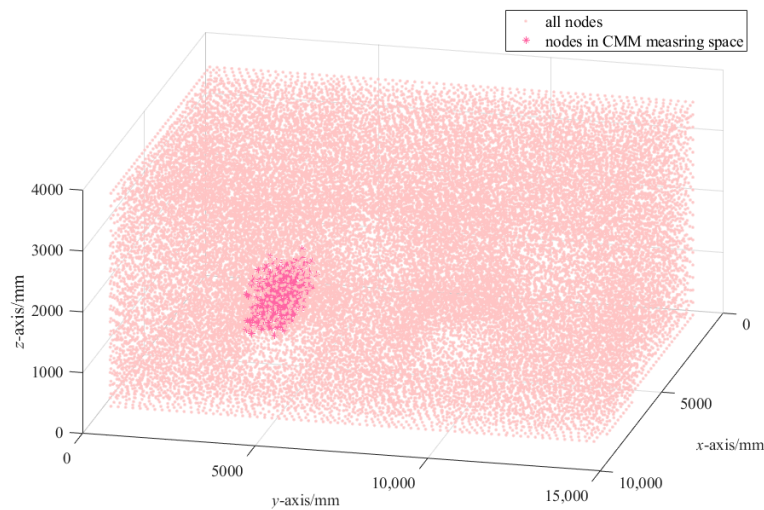


Figure 9. Selection of training sample data for the non-uniform-temperature field model.

In the establishment of the temperature field at time t , based on the above characteristics of the temperature change in the CMM measurement space, the temperature field data of the two cases (complex constant-temperature environment and natural convection environment) at $t = 56$ min were divided into training and test samples at a ratio of 8:2. Training was then carried out by substituting the training data into the non-uniform-temperature field model established based on the RBF neural network (Equation (8)). The temperature distributions at $t = 56$ min in the complex constant-temperature and natural-convection environments are shown in Figure 10. The training errors obtained from the test samples are listed in Tables 1 and 2. In the table, AVG denotes average; MSE denotes mean squared error; RMSE denotes root mean squared error. The model yielded a mean error and root mean squared error < 0.04 °C in the temperature estimation of stratified sampling points and random sampling points in both environments. The results indicated that a non-uniform-temperature field could be established using this model.

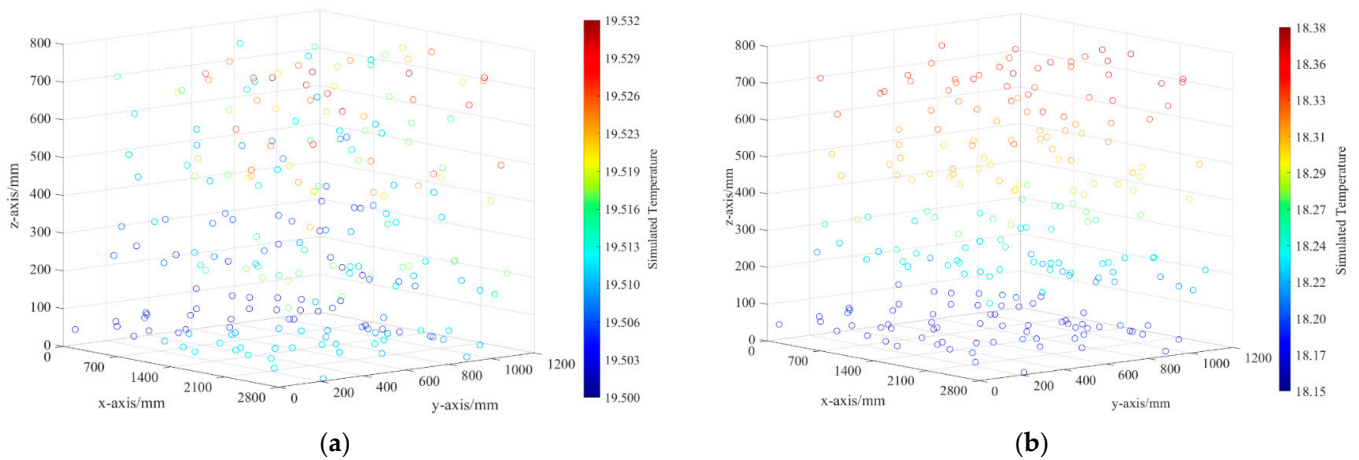


Figure 10. Temperature distributions at $t = 56$ min in two different cases: (a) complex constant-temperature environment; (b) natural convection environment.

Table 1. Training error obtained in the complex constant-temperature environment.

Sampling Method	AVG/°C	MSE/°C ²	RMSE/°C
Stratified sampling	9.1×10^{-3}	2.6×10^{-4}	1.6×10^{-2}
Random sampling	1.8×10^{-2}	1.4×10^{-3}	3.7×10^{-2}

Table 2. Training error obtained in the natural convection environment.

Sampling Method	AVG/°C	MSE/°C ²	RMSE/°C
Stratified sampling	1.5×10^{-2}	6.9×10^{-4}	2.6×10^{-2}
Random sampling	1.6×10^{-2}	5.9×10^{-4}	2.4×10^{-2}

For the model considering time t , the initial conditions for the numerical simulation were changed by increasing the initial temperature to 20 °C. The new temperature data were obtained based on the effects of solar radiation. The temperature field data of the air-conditioned constant-temperature environment and natural convection environment were substituted into the non-uniform-temperature field model established based on the RBF neural network. The training results are shown in Figure 11, and the training errors are listed in Tables 3 and 4. The standard error of the mean and root mean squared error of the model were less than 0.02 °C for temperature data with intervals of 5 and 10 min in both environments. The training error decreased as the time interval decreased. The model could more accurately estimate the temperature distribution in a natural convection environment (the training error reached 10^{-3} orders of magnitude) than the complex temperature distribution in an air-conditioned constant-temperature environment. The

results indicated that the model could simulate a time-varying, non-uniform-temperature field. In addition, accuracy was higher when the time variable was substituted into the data as a training sample. A shorter time interval corresponds to more information in the time dimension obtained under the fixed conditions of the other dimensions of the sample data and a smaller training error.

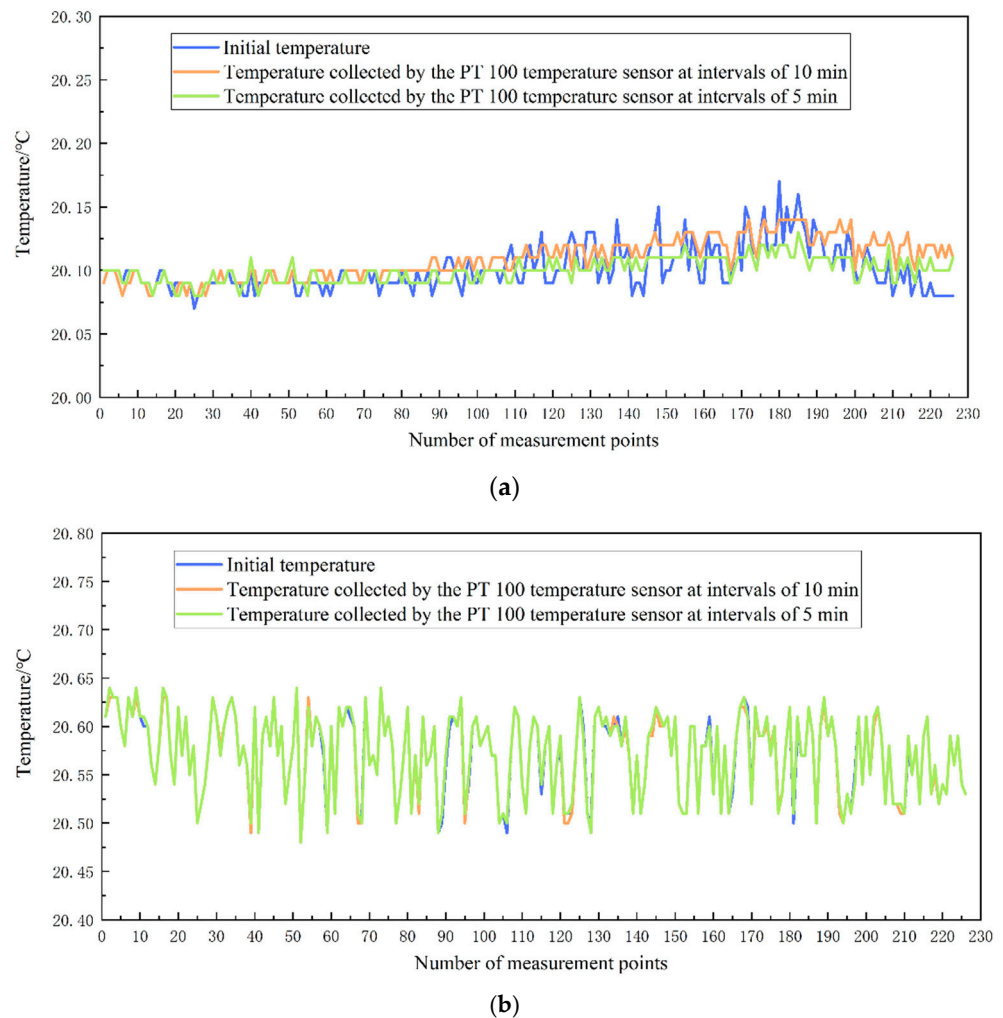


Figure 11. Training results at $t = 56$ min in two different cases: (a) complex constant-temperature environment; (b) natural convection environment.

Table 3. Training error obtained in the complex fixed temperature environment.

Sampling Method	AVG/°C	MSE/°C ²	RMSE/°C
10 min interval	1.2×10^{-2}	2.6×10^{-4}	1.6×10^{-2}
5 min interval	9.4×10^{-3}	1.8×10^{-4}	1.3×10^{-2}

Table 4. Training error obtained in the natural convection environment.

Sampling Method	AVG/°C	MSE/°C ²	RMSE/°C
10 min interval	1.8×10^{-3}	1.8×10^{-5}	4.2×10^{-3}
5 min interval	1.3×10^{-3}	1.3×10^{-5}	3.6×10^{-3}

4. Results and Discussion

The temperature-compensation study was based on a laser-tracing multi-station measurement system for the CMM error measurements. To verify the feasibility and accuracy

of the temperature-compensation model, a laser-tracing multi-station measurement simulation experiment was designed. A laser tracer was used to measure the errors of the CMM with a measurement area of 5000 mm × 2500 mm × 2000 mm. The measurement points were planned in space (4000 mm × 2500 mm × 2000 mm; Figure 12). The steps in each axial direction were set as follows: x = 500 mm, y = 625 mm, and z = 500 mm. In total, 225 measurement points were set (9 × 5 × 5 = 225). Four stations were set near the beginning of the X-axis direction. The coordinates of these four stations are listed in Table 5. The laser tracer was successively placed at these four stations for measurements. A round-trip measurement was performed for all measuring points at each station, and 4 × 449 data points were generated. To ensure measurement accuracy and integrity, it was assumed that the measurement time at each point was 10 s (starting from the movement of the cat’s eye and ending after the measurement at a point). The measurement times of all measurement points were added to the station-shifting time to obtain the measurement time for each station (90 min). The total measurement time at all the four stations was 360 min (90 × 4 = 360 min). The temperature distribution and variation in the simulation were given by the model obtained in the previous simulation, including the coordinates in the 3D Cartesian coordinate system, time, and other independent variables.

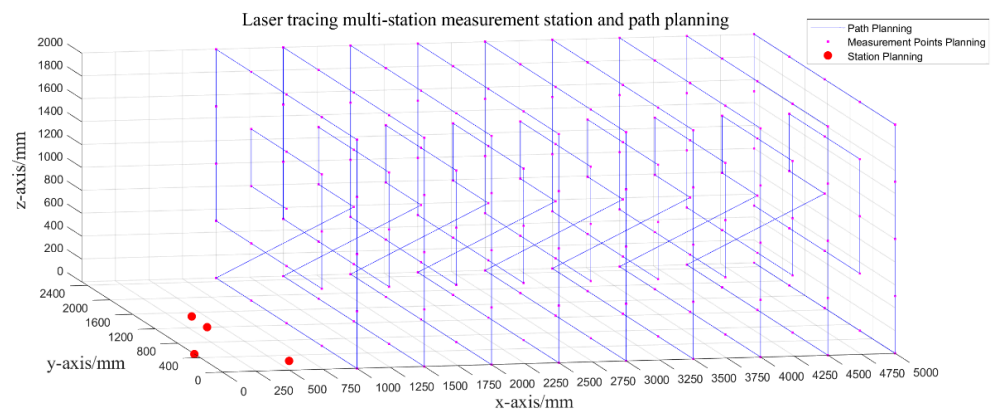


Figure 12. Simulation environment setting.

Table 5. Laser-tracer station settings.

	X/mm	Y/mm	Z/mm
Station 1	0	500	0
Station 2	600	250	0
Station 3	400	1500	0
Station 4	200	750	150

4.1. RBF-Based Non-Uniform-Temperature Field Model for Range-Segmented Temperature Estimation

The correctness of the RBF non-uniform-temperature field model was verified. Because of the movement of each axis in the multi-station measurement experiment, it was impossible to place a temperature sensor at a fixed point inside the measurement space of the CMM. Therefore, temperature-measurement points were set at equal spacing along the boundary of the measurement space. Sixty stationary temperature sensors were placed at the boundary of the CMM measurement range (Figure 13). The spacing was consistent with the steps adopted to plan the measurement points. Temperature data were saved every 5 min, and temperature data containing location and time information were obtained. Additionally, one measurement point was set for each laser tracer and catenary device. Among them, the temperature data of 60 sampling points set at the boundary of the measurement range and the laser-tracer station data are accurate data obtained by fitting calculation based on ANSYS FLUENT software as training samples. The remaining 165 sampling

points in the CMM measurement space, except the boundary points, are the data calculated by network training with the multi-order fitting model as the test samples.

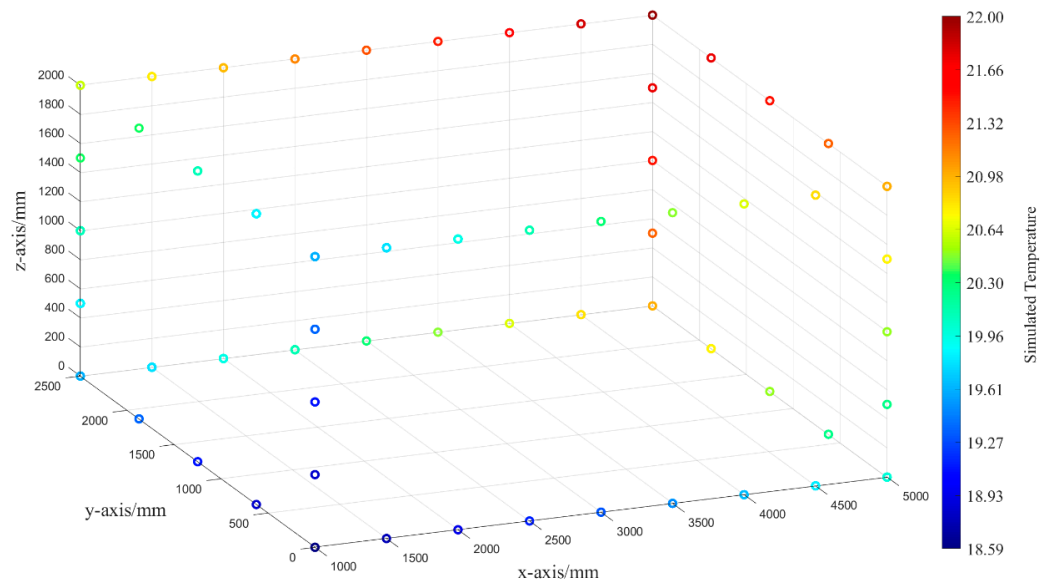


Figure 13. Boundary temperature-measurement point setting.

The coordinates, temperature, and time data of the boundary temperature-measurement points, four stations, and the measurement points at stations 1–3 were used as training samples and substituted into the RBF non-uniform-temperature field model for training. The temperatures at the measurement points at Station 4 were used as the test samples. The results are presented in Figure 14. The temperature error of the test samples was within 0.5 °C. The average absolute error $e_{MAE} = 0.09$ °C, and $e_{RMSE} = 0.13$ °C, which were lower than the measurement error of common sensors. Subsequently, the temperature estimation in the CMM workspace can be achieved using the RBF non-uniform-temperature field model.

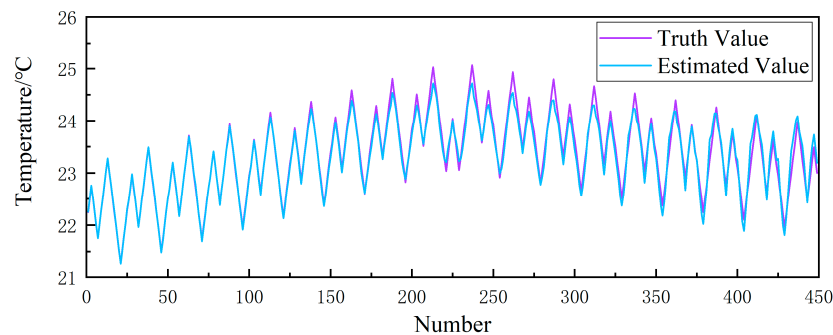


Figure 14. Temperature estimation of the measurement points at Station 4.

Based on the experimental conditions above, the distance between the laser tracer and each measurement point at each station was determined as the distance measurement value. The number and length of the segments of the measurement optical path were then determined using the length of the measurement optical path and the span in each axis direction. The data of each dimension at the temperature-measurement points were substituted into the RBF non-uniform-temperature field model, and the temperature at the midpoint of each segment was obtained as the temperature at the corresponding segment.

To simplify the experimental device and reduce redundant data, the sensitivity of the segmented temperature to the data at each type of measurement point was analyzed. Training samples with and without the added data of the boundary temperature-measurement

points were explored. That is, the data obtained at all four stations and those obtained at Stations 1–3 were used to train the model for comparison. The midpoint temperature data of each measurement point in Station 4 were used as the test samples. The temperature errors are shown in Figure 15 and are listed in Table 6. The comparison results indicate that the addition of the sample data of the boundary points had little effect on the training error of the test samples. In summary, the segment midpoint temperature estimation can also be achieved without using boundary temperature-measurement point data.

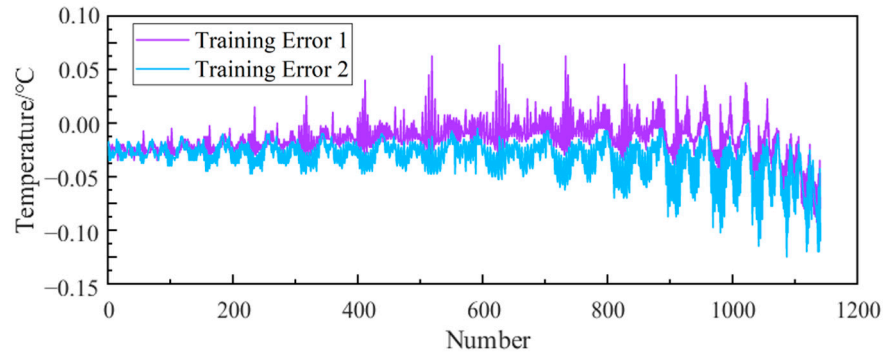


Figure 15. Comparison of training error for two training samples.

Table 6. Comparison of training error for two training samples.

Training Samples	$e_{MAE}/^{\circ}C$	$e_{MSE}/^{\circ}C^2$	$e_{RMSE}/^{\circ}C$
Boundary points, stations, and measurement points	5.79×10^{-2}	6.36×10^{-3}	7.98×10^{-2}
Stations and measurement points	5.19×10^{-2}	6.21×10^{-3}	7.88×10^{-2}

The sensitivity of the segmented temperature to the measurement point data obtained from the tracer and cat’s eye was further analyzed. A comparative study was conducted using training samples with and without temperature data from four stations. The test samples were segmented at the midpoint temperatures measured at each station (Figure 16 and Table 7). The average absolute temperature error e_{MAE} was reduced from 0.0255 °C to 0.00718 °C after substituting the temperature data of each station. Thus, the error was reduced by more than 50%. Therefore, for the temperature-compensation model in this study, it was necessary to arrange the temperature-measurement points at each station. The temperature data at each station contained only the temperature information of the four points. The location information contained was limited, so it was impossible to estimate the temperature at other locations in the measurement range using the temperature data at each station.

In summary, the temperature at any point in the CMM workspace can be estimated using an RBF non-uniform-temperature field model with coordinates and time information as the input. This model can be used to estimate the temperature at the midpoint of a laser-tracer measurement optical path segment. Temperature sensors at the laser tracer and cat’s eye can be used to obtain real-time temperatures at stations and measurement points, thus facilitating temperature compensation for the laser-tracing multi-station measurement technique.

Table 7. Comparison of the training errors for two training samples.

Training Samples	$e_{MAE}/^{\circ}C$	$e_{MSE}/^{\circ}C^2$	$e_{RMSE}/^{\circ}C$
Stations and measurement points	7.18×10^{-3}	9.44×10^{-5}	9.72×10^{-3}
Measurement points	2.55×10^{-2}	1.12×10^{-3}	3.34×10^{-2}

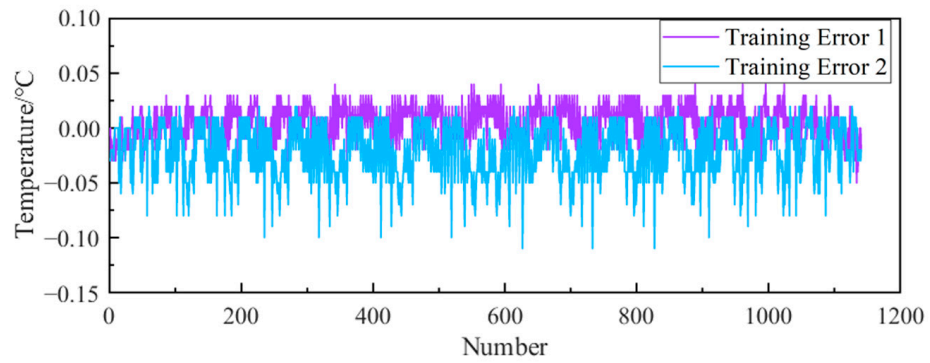


Figure 16. Comparison of the training errors for two training samples.

4.2. Effect of the Non-Uniform-Temperature Field on CMM Volumetric Error

The simulation experiment was set up as shown in Figure 12. The distances between the four stations and each measurement point were determined based on the simulation results. As described in the previous section, two temperature-measurement points of the laser tracer and cat’s eye were selected, and the real-time temperatures of the stations and measurement points were obtained. The compensation results of the non-uniform-temperature field model in this study were calculated using the segments along the measurement optical path and the estimated midpoint temperature of each segment.

The influence of temperature compensation on the accuracy improvement of the laser-tracing multi-station measurement technology was explored in the following three cases. First, the overall temperature was set to 20 °C. Second, according to the traditional method, the arithmetic mean of the station temperature at the beginning and end of the measurement process at each station was used as the average temperature in the overall measurement space at that station. The measurement errors of the temperature sensors were considered; however, an uneven temperature distribution was not considered. Third, the non-uniform temperature distribution and variation in temperature with time were considered, and the temperature-compensation method proposed in this study was adopted. The measurement errors of the temperature sensors were also considered. To solve volumetric errors, a comparison of the errors caused by non-standard temperatures in the three simulation cases is shown in Tables 8–10. After the errors along three axes were synthesized, the average absolute error caused by the introduction of temperature without temperature compensation reached 1.118 μm. Therefore, a temperature compensation was applied to the multi-station measurement system. The average absolute error caused by the introduction of temperature was reduced to 0.313 μm using the conventional compensation method and reached 0.208 μm after temperature compensation using the method proposed in this study. In summary, the measurement error caused by the ambient temperature deviation from 20 °C, and the non-uniform-temperature field can be effectively reduced by the temperature-compensation method proposed in this study. Compared with the conventional temperature-compensation method, the proposed temperature-compensation method improved the accuracy of the measurement of volumetric errors of large-scale CMMs using the laser-tracing multi-station technique in a non-uniform-temperature field by 33.5%.

Table 8. Errors in uncompensated temperature cases.

	X-Direction/μm	Y-Direction/μm	Z-Direction/μm
MAE	0.378	0.339	0.996
MAX	1.230	1.530	5.990

Table 9. Errors in the compensation temperature case based on the first and last mean values.

	X-Direction/ μm	Y-Direction/ μm	Z-Direction/ μm
MAE	0.147	0.129	0.244
MAX	0.526	0.547	2.040

Table 10. Errors in the temperature-compensation case based on RBF model in a non-uniform-temperature field.

	X-Direction/ μm	Y-Direction/ μm	Z-Direction/ μm
MAE	0.046	0.019	0.202
MAX	0.195	0.087	0.168

4.3. Effect of the Non-Uniform-Temperature Field on the Geometric Error of CMM

The range values and volumetric errors were determined based on three cases before and after temperature compensation. The geometric error could then be solved using a quasi-rigid body model, an elastic network algorithm, and QR decomposition. The obtained results were used to explore the effect of the non-uniform-temperature field on the geometric error of the CMM. The errors caused by the positioning errors in the three cases are shown in Figure 17. Under the simulation experimental conditions in this study, the maximum measurement error of the positioning error introduced by the temperature in each axis direction reached nearly 0.6 μm when the temperature deviation and non-uniform-temperature field were not compensated. The accuracy of the positioning error on each axis improved after temperature compensation using both methods. The proposed method outperformed the conventional method in terms of temperature compensation. In summary, the error caused by the temperature effect could be largely reduced by compensating for the temperature error using the laser-tracing multi-station technique. Compared with the traditional mean compensation, the compensation of the non-uniform-temperature field was more effective, as confirmed by the positioning errors in X-axis and Y-axis directions. The positioning error compensation effect on Z-axis was different from that on X-axis and Y-axis, mainly because of the position setting of the laser tracer.

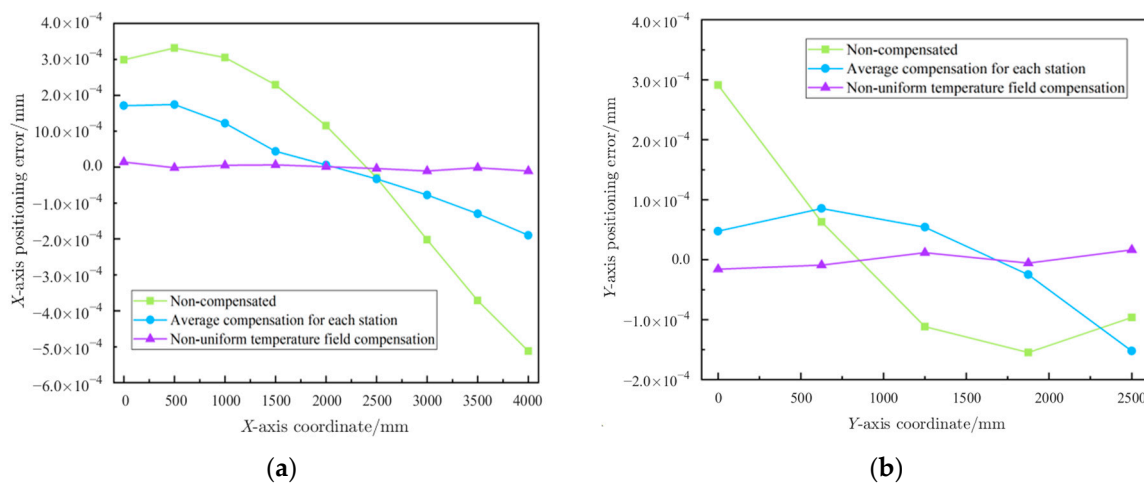
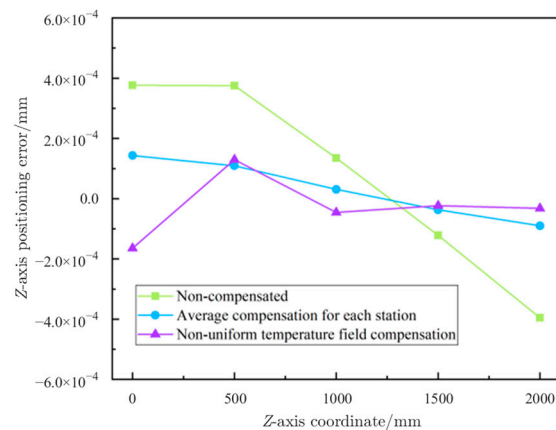


Figure 17. Cont.



(c)

Figure 17. Accuracy improvement of the positioning error of each axis before and after temperature compensation: (a) X-axis; (b) Y-axis; (c) Z-axis.

5. Conclusions

In this study, a laser-tracer multi-station measurement method under a non-uniform-temperature field was proposed, and the laser-tracer multi-station model was improved. After the measurement optical path was segmented, the ambient temperature at specified points was estimated based on RBF neural network and substituted into the laser-tracing multi-station measurement model for temperature compensation. The following conclusions were drawn from a series of simulations. First, the RBF non-uniform-temperature field model can be used to estimate the temperature at any point. Second, with the improved model, the temperature of each segment of the measurement optical path can be estimated by setting the temperature-measurement points at two locations: the laser tracer and the cat's eye. Third, with the laser-tracing multi-station measurement technique for volumetric error and geometric error of large-scale CMMs, the temperature-compensation method proposed in this study can reduce the measurement error caused by the deviation of ambient temperature from 20 °C and the non-uniform-temperature field. Compared with the traditional temperature-compensation method, the method proposed in this study can improve the measurement accuracy of the volumetric error of a large-scale CMM using laser-tracing multi-station technology in a non-uniform-temperature field by 33.5%. This study provides a new method for improving the accuracy of laser-tracer multi-station measurement systems.

Author Contributions: Conceptualization, H.C.; methodology, H.C.; software, M.S.; validation, H.C., A.Z., M.S. and C.L.; formal analysis, A.Z.; investigation, H.C.; resources, H.C.; data curation, M.S.; writing—original draft preparation, M.S.; writing—review and editing, A.Z. and H.W.; visualization, A.Z.; supervision, H.C. and Z.L.; project administration, H.C.; funding acquisition, Z.S. All authors have read and agreed to the published version of the manuscript.

Funding: This research was supported by National Natural Science Foundation of China (NSFC) under Grant No. 52175491 and National Major Scientific Research Instrument Development Project under Grant No. 52227809.

Institutional Review Board Statement: Not applicable.

Informed Consent Statement: Not applicable.

Data Availability Statement: Data underlying the results presented in this paper are not publicly available at this time but may be obtained from the authors upon reasonable request.

Conflicts of Interest: The authors declare no conflict of interest.

References

1. Zhang, G.X. The development trend of coordinate measuring machine. *China Mech. Eng.* **2000**, *11*, 231–235.
2. Lin, H.; Keller, F.; Stein, M. Influence and compensation of CMM geometric errors on 3D gear measurements. *Measurement* **2020**, *151*, 107110. [\[CrossRef\]](#)
3. Aguado, S.; Samper, D.; Santolaria, J.; Aguilar, J.J. Towards an effective identification strategy in volumetric error compensation of machine tools. *Meas. Sci. Technol.* **2012**, *6*, 207. [\[CrossRef\]](#)
4. Aguado, S.; Santolaria, J.; Samper, D.; Aguilar, J.J. Influence of measurement noise and laser arrangement on measurement uncertainty of laser tracker multilateration in machine tool volumetric verification. *Precis. Eng.* **2013**, *37*, 929–943. [\[CrossRef\]](#)
5. Wang, J.D.; Guo, J.J. Algorithm for detecting volumetric geometric accuracy of nc machine tool by laser tracker. *Chin. J. Mech. Eng.* **2013**, *26*, 166–175. [\[CrossRef\]](#)
6. Schwenke, H.; Schmitt, R.; Jatzkowski, P.; Warmann, C. On-the-fly calibration of linear and rotary axes of machine tools and CMMs using a tracking interferometer. *CIRP Ann.-Manuf. Technol.* **2009**, *58*, 477–480. [\[CrossRef\]](#)
7. Camboulives, M.; Lartigue, C.; Bourdet, P.; Salgado, J. Calibration of a 3D working space by multilateration. *Precis. Eng.* **2016**, *44*, 163–170. [\[CrossRef\]](#)
8. Yu, J.B. Analysis and discussion on the calibration process of CMM. *Metrol. Test. Technol.* **2022**, *49*, 76–78.
9. Hennebelle, F.; Coorevits, T.; El Asmai, A.; Goutagneux, F.; Vincent, R. Impact of thermal gradients on the geometry correction of a bridge coordinate measuring machine. *Meas. Sci. Technol.* **2021**, *32*, 025002. [\[CrossRef\]](#)
10. Meirbek, M.; Huang, M.F.; Selim, B. Thermal influences as an uncertainty contributor of the coordinate measuring machine (CMM). *Int. J. Adv. Manuf. Technol.* **2020**, *111*, 537–547.
11. Štrbac, B.; Ačko, B.; Havrlišan, S.; Matin, I.; Savković, B.; Hadžistević, M. Investigation of the effect of temperature and other significant factors on systematic error and measurement uncertainty in CMM measurements by applying design of experiments. *Measurement* **2020**, *158*, 107692. [\[CrossRef\]](#)
12. Joo, K.; Ellis, D.J.; Spronck, W.J.; Schmidt, R.H.M. Real-time wavelength corrected heterodyne laser interferometry. *Precis. Eng.* **2010**, *35*, 38–43. [\[CrossRef\]](#)
13. He, M.Z.; Li, J.S.; Miao, D.J. Equivalent common path method in large-scale laser comparator. *Natl. Inst. Metrol.* **2015**, *9446*, 974–980.
14. Tang, X.J.; Zhu, X.S.; Zheng, L.Y. Configuration optimization of laser tracker stations for large-scale components in non-uniform temperature field using monte-carlo method. *Procedia CIRP* **2016**, *56*, 261–266.
15. Li, T.; Li, J.S.; Miao, D.J.; Li, L.; Liu, X. Study of temperature states influence on the accuracy of large size measuring devices. *J. Metrol.* **2019**, *40*, 975–979.
16. Aguilar, J.J.; Acero, R.; Brosed, J.F.; Santolaria, J. Development of a High Precision Telescopic Instrument Based on Simultaneous Laser Multilateration for Machine Tool Volumetric Verification. *Sensors* **2020**, *20*, 3798. [\[CrossRef\]](#) [\[PubMed\]](#)
17. Huang, X.; Zeng, Z.P. An error similarity-based error-compensation method for measurement in the nonuniform temperature field. *Meas. Sci. Technol.* **2020**, *31*, 8.
18. Marco, P.; Milena, A.; Massimo, Z. Improved Acoustic Thermometry for Long-Distance Temperature Measurements. *Sensors* **2023**, *23*, 1638. [\[CrossRef\]](#)
19. Wu, J.; Zhang, C.P.; Pan, Z.X.; Zhang, X.; Guo, R. Precision compensation method for visual measurement based on nonuniform refractive index field reconstruction. *Appl. Opt.* **2023**, *62*, 2300–2309. [\[CrossRef\]](#)
20. Chen, H.F.; Jiang, B.; Shi, Z.Y.; Sun, Y.; Song, H.; Tang, L. Uncertainty modeling of the spatial coordinate error correction system of the CMM based on laser tracer multi-station measurement. *Meas. Sci. Technol.* **2019**, *30*, 025007. [\[CrossRef\]](#)
21. Downs, M.J.; Birch, K.P. An updated Edlén equation for the refractive index of air. *Metrologia* **1993**, *30*, 155–162.
22. Zhou, X.; Wang, Q.; Nong, N.Z.; Miao, Z.; Wu, W.G. Three-dimensional temperature field reconstruction algorithm based on RBF neural network. *Instrum. Tech. Sens.* **2013**, *5*, 99–102.
23. Chen, H.F.; Zheng, B.W.; Shi, Z.Y.; Sun, Y.; Long, C.; Yang, Z. CMM spatial coordinate correction method based on laser tracker multi-station measurement. *Chin. Laser* **2017**, *44*, 197–204.
24. Zhang, G.X. *Coordinate Measuring Machines*, 1st ed.; Tianjin University Press: Tianjin, China, 1999; pp. 354–364.
25. Chen, H.F.; Sun, M.Y.; Gao, Y.; Shi, Z.Y.; Wang, G.Y.; Lu, W.G.; Song, H.X. Method of solving geometric error of large-scale CMM using elastic net algorithm. *China Mech. Eng.* **2022**, *33*, 1077–1083.
26. Launder, B.E.; Spalding, D.B. *Lectures in Mathematical Models of Turbulence*, 1st ed.; Academic Press: London, UK, 1972; pp. 151–190.
27. Yao, X.H.; Li, R.; Wang, L.X.; Ren, Z. Numerical simulation analysis of air-conditioned environment in winter and summer of a building atrium in Beijing. *Fluid Mach.* **2016**, *44*, 72–76.

Disclaimer/Publisher’s Note: The statements, opinions and data contained in all publications are solely those of the individual author(s) and contributor(s) and not of MDPI and/or the editor(s). MDPI and/or the editor(s) disclaim responsibility for any injury to people or property resulting from any ideas, methods, instructions or products referred to in the content.